Limit Analysis with the Dual Affine Scaling Algorithm

Knud D. Andersen

Edmund Christiansen

Department of Mathematics and Computer Science

Odense University

Campusvej 55, DK–5230 Odense M, Denmark

e-mail: edc@imada.ou.dk

February 16, 1995

Abstract

The collapse state of a rigid plastic material with the linearized Mises yield condition is computed. We use an infeasible point variant of the dual affine scaling algorithm for linear programming which is extremely efficient for this large sparse and ill conditioned problem.

For a classical test problem we obtain better results than previously, both for the limit load and for the collapse fields, thus setting a new standard for computations in limit analysis.

Keywords: Limit analysis, plasticity, finite element method, linear programming, interior point methods.

Short title: Limit analysis with dual scaling.

1 Introduction

In limit analysis we consider a rigid plastic material subject to a fixed load distribution. The object is to find the maximum multiple of this load distribution that the solid can be subject to before collapse occurs. We also want to find the collapse mechanism, i.e. the fields for stresses and plastic flow in the collapse state.

Let $\Omega \subseteq \mathbb{R}^3$ be the domain occupied by the solid. Part of the boundary $S \subseteq \partial\Omega$ is kept fixed, i.e. $\boldsymbol{u} = \boldsymbol{0}$ on S, where $\boldsymbol{u}$ denotes the plastic flow field. The rest of the boundary $T \subseteq \partial\Omega$ is subject to surface forces, $\boldsymbol{g} = \boldsymbol{g}(\boldsymbol{x})$ for $\boldsymbol{x} \in T$. The volume forces are denoted $\boldsymbol{f} = \boldsymbol{f}(\boldsymbol{x})$ for $\boldsymbol{x} \in \Omega$. The work rate of the external forces combined with a virtual plastic flow field $\boldsymbol{u}$ is

$$F(\boldsymbol{u}) = \int_\Omega \boldsymbol{f} \cdot \boldsymbol{u} \; d\boldsymbol{x} + \int_T \boldsymbol{g} \cdot \boldsymbol{u} \; ds. \tag{1}$$

The internal work rate is given by

$$\begin{aligned} a(\boldsymbol{\sigma}, \boldsymbol{u}) &= \int_\Omega \sum_{i,j} \sigma_{ij}\varepsilon_{ij} \; d\boldsymbol{x} && (2) \\ &= -\int_\Omega (\boldsymbol{\nabla} \cdot \boldsymbol{\sigma}) \cdot \boldsymbol{u} \; d\boldsymbol{x} + \int_T (\boldsymbol{\nu} \cdot \boldsymbol{\sigma}) \cdot \boldsymbol{u} \; ds && (3) \end{aligned}$$

where $\boldsymbol{\nu}$ is the outward normal, $\boldsymbol{\sigma}$ is the stress tensor, and $\boldsymbol{\varepsilon} = \boldsymbol{\varepsilon}(\boldsymbol{u})$ denotes the strain rate tensor given by

$$\varepsilon_{ij} = \frac{1}{2}\left(\frac{\partial u_i}{\partial x_j} + \frac{\partial u_j}{\partial x_i}\right). \tag{4}$$

The equality between (2) and (3) follows from Green's formula. For the mathematical details of the model we refer to [7].

The equation of equilibrium between the stress tensor $\boldsymbol{\sigma}$ and the external forces $(\boldsymbol{f}, \boldsymbol{g})$ is the equation of virtual work rate:

$$a(\boldsymbol{\sigma}, \boldsymbol{u}) = F(\boldsymbol{u}) \quad \text{for all } \boldsymbol{u} \text{ with } \boldsymbol{u} = \boldsymbol{0} \text{ on } T. \tag{5}$$

If we equate (1) and (3) we get the classical form of the equilibrium equation.

In addition to the equilibrium equation the stress tensor must satisfy the yield condition. In this paper we shall assume the von Mises yield condition for a homogeneous material but the method described is completely general. In 3 space dimensions the von

Mises condition is

$$(\sigma_{11}-\sigma_{22})^2+(\sigma_{22}-\sigma_{33})^2+(\sigma_{33}-\sigma_{11})^2+6(\sigma_{12}^2+\sigma_{23}^2+\sigma_{31}^2)\leq 2\sigma_0^2, \tag{6}$$

where σ_0 is the yield stress in simple tension. The condition (6) must be satisfied at each point of the solid. Note that the yield condition is insensitive to the addition of any tensor of the form $\varphi \boldsymbol{I}$, where $\boldsymbol{I}$ is the unit tensor, and φ is any scalar function. Hence the set K of admissible stress tensors is unbounded. This is a general complication in limit analysis. As we shall see below, there is a dual property of the plastic flow $\boldsymbol{u}$: It must be divergence free, $\boldsymbol{\nabla}\cdot\boldsymbol{u}=0$, in order to have finite energy dissipation rate.

The problem of limit analysis can now be formulated in the following very intuitive way. The limit multiplier λ^* for the pair of forces $(\boldsymbol{f},\boldsymbol{g})$ is the smallest upper bound of all values λ, for which there exists an admissible stress tensor $\boldsymbol{\sigma}$ which is in equilibrium with the forces $(\lambda\boldsymbol{f},\lambda\boldsymbol{g})$:

$$\lambda^* = \sup\{\lambda|\exists\boldsymbol{\sigma}\in K : a(\boldsymbol{\sigma},\boldsymbol{u})=\lambda F(\boldsymbol{u})\ \forall\boldsymbol{u}\} \tag{7}$$

$$= \sup_{\sigma\in K}\min_{F(u)=1} a(\boldsymbol{\sigma},\boldsymbol{u}). \tag{8}$$

Equation (7) is known as the *static principle* of limit analysis. The equality between (7) and (8) is a consequence of the fact that the linear map $\boldsymbol{u}\mapsto a(\boldsymbol{\sigma},\boldsymbol{u})$ is either unbounded on the affine subspace $\{\boldsymbol{u}|F(\boldsymbol{u})=1\}$ or proportional to F.

Reversing the order of maximum and minimum in (8) leads to the dual problem, also known as the *kinematic principle* of limit analysis:

$$\lambda^* = \inf_{F(u)=1}\sup_{\sigma\in K} a(\boldsymbol{\sigma},\boldsymbol{u}) = \inf_{F(u)=1} D(\boldsymbol{u}) \tag{9}$$

where

$$D(\boldsymbol{u}) = \sup_{\sigma\in K} a(\boldsymbol{\sigma},\boldsymbol{u}) \tag{10}$$

is the total energy dissipation rate associated with the flow field $\boldsymbol{u}$.

It is proved in [7] that the static and the kinematic principles give the same value for the collapse multiplier and that there exists a saddle point $(\boldsymbol{\sigma}^*,\boldsymbol{u}^*)$ such that the following holds for all admissible stress tensors, $\boldsymbol{\sigma}\in K$, and all $\boldsymbol{u}$ satisfying the boundary condition

$\boldsymbol{u} = \boldsymbol{0}$ on S and normalized to $F(\boldsymbol{u}) = 1$:

$$a(\boldsymbol{\sigma}, \boldsymbol{u}^*) \leq \lambda^* = a(\boldsymbol{\sigma}^*, \boldsymbol{u}^*) \leq a(\boldsymbol{\sigma}^*, \boldsymbol{u}) \tag{11}$$

$\boldsymbol{\sigma}^*$ and $\boldsymbol{u}^*$ are the collapse fields for stresses and plastic flow. Note that

$$\lambda^* = D(\boldsymbol{u}^*) = \max_{\sigma \in K} \int_\Omega \sum_{i,j} \sigma_{ij} \varepsilon_{ij}(\boldsymbol{u}^*) d\boldsymbol{x}. \tag{12}$$

This leads to the principle of complementary slackness: At each point $\boldsymbol{x} \in \Omega$ where $\boldsymbol{\varepsilon}(\boldsymbol{u}^*)$ is non–zero, the collapse stress tensor $\boldsymbol{\sigma}^*$ must be at the yield surface at a point with $\boldsymbol{\varepsilon}(\boldsymbol{u}^*)$ as the outward normal.

2 The Discrete Problem

The discretization of the saddle point problem (8)–(9) by the finite element method is described in [6]. Finite element spaces are chosen for stresses and flow. Let $h > 0$ indicate the linear mesh size of the grid. The discrete stress tensor $\boldsymbol{\sigma}_h$ and flow $\boldsymbol{u}_h$ are then represented through their nodal values, i.e. coordinates w.r.t. the usual finite element bases. Let $\boldsymbol{x} = (x_n)_{n=1}^N$ and $\boldsymbol{y} = (y_m)_{m=1}^M$ denote the coordinates representing $\boldsymbol{\sigma}_h$ and $\boldsymbol{u}_h$ respectively. Then the external and internal work rates may be written

$$a(\boldsymbol{\sigma}_h, \boldsymbol{u}_h) = \sum_{m=1}^M \sum_{n=1}^N y_m x_n a_{mn} = \boldsymbol{y}^T \boldsymbol{A} \boldsymbol{x} = \boldsymbol{x}^T \boldsymbol{A}^T \boldsymbol{y} \tag{13}$$

$$F(\boldsymbol{u}_h) = \sum_{m=1}^M y_m b_m = \boldsymbol{b}^T \boldsymbol{y}. \tag{14}$$

The discrete form of the yield condition $\boldsymbol{\sigma}_h \in K$ becomes $\boldsymbol{x} \in K_d$, where K_d is a closed convex, in general unbounded, subset of $\mathbb{R}^N$. The corresponding energy dissipation rate of $\boldsymbol{u}_h$ is

$$D_d(\boldsymbol{y}) = \max_{\boldsymbol{x} \in K_d} \boldsymbol{x}^T \boldsymbol{A}^T \boldsymbol{y}. \tag{15}$$

With this notation the discrete form of the static principle (7) is a finite dimensional

optimization problem:

$$\begin{aligned} \lambda_h^* = \quad & \max \quad \lambda \\ & \boldsymbol{A}\boldsymbol{x} = \lambda \boldsymbol{b} \\ & \boldsymbol{x} \in K_d \end{aligned} \tag{16}$$

while the kinematic principle takes the form

$$\begin{aligned} \lambda_h^* = \quad & \min \quad D_d(\boldsymbol{y}) \\ & \boldsymbol{b}^T \boldsymbol{y} = 1. \end{aligned} \tag{17}$$

The optimization problems (16) and (17) are dual problems and yield the same value.

We focus on the static form (16) and use the classical approach of linearizing the yield condition, in spite of the fact that it is now feasible to approach (16) by convex programming methods. At the cost of the linearization we shall be able to solve with a finer grid and hence obtain a more detailed collapse solution than seen before. One reason for this is that the efficiency of the algorithm used here shows very little sensitivity to the addition of sparse linear constraints.

After linearization of the yield condition the discrete static formulation (16) becomes a linear programming problem of the form

$$\begin{aligned} \lambda_h^* = \quad & \max \lambda \\ & \boldsymbol{A}\boldsymbol{x} = \boldsymbol{b}\lambda \\ & \boldsymbol{B}\boldsymbol{x} \leq \boldsymbol{c}. \end{aligned} \tag{18}$$

The equality constraints correspond to the equilibrium equation. The $M \times N$ matrix $\boldsymbol{A}$ has the usual finite element structure, although non–symmetric, while the M–vector $\boldsymbol{b}$ may be a "full" vector, depending on the load. The inequality constraints $\boldsymbol{B}\boldsymbol{x} \leq \boldsymbol{c}$ are the linearized yield condition. They are very sparse and of a particularly simple block diagonal structure: Each inequality involves only the nodal values corresponding to a single node in the finite element grid.

The simplex method has been an important factor in the development of limit analysis (see for example [4], [2], [6]) for use with mixed finite elements and the discussion in [5, page 172]. However, in our experience the simplex method is not well suited for continuum problems, because of its extreme-point property. If a whole face is optimal, or if the feasible set is very "flat" near the optimum, then the simplex method will always choose an extreme-point solution (a basis solution in LP–terminology). This solution need not be

physically consistent from node to node. This means that the optimal value, the collapse multiplier, is well determined, but that the collapse fields are poorly determined in the case of non–uniqueness or ill–conditioning, both of which typically occur in limit analysis. This is reported in [6].

Starting with Karmarkar's polynomial-time algorithm [11] several efficient interior-point methods for linear programming have been introduced. In [8], [9] the *Primal Affine Scaling Algorithm* was applied to (18) transformed to LP–standard form. It was known then that the *Dual Affine Scaling Algorithm*, which essentially approaches the dual form of (18) by the primal algorithm, offers several computational advantages for most problems (see below). However, in the problem (18) most of the variables are free, i.e. without upper or lower bound. This means that the feasible set for the dual problem has empty interior, preventing use of the dual algorithm.

3 Solution Algorithm

We rewrite the discrete static formulation (18) in LP–standard form by introducing slack variables and duplicating free variables:

$$\min_{\boldsymbol{x}\in X_p} \boldsymbol{c}^T\boldsymbol{x}, \quad X_p = \{\boldsymbol{x} \in \mathbb{R}^n \mid \boldsymbol{A}\boldsymbol{x} = \boldsymbol{b}, \boldsymbol{x} \geq \boldsymbol{0}\}\,. \tag{19}$$

In (19) $\boldsymbol{A}$ and $\boldsymbol{b}$ are not the same as in (18). An interior point for (19) is a vector $\boldsymbol{x} \in \mathbb{R}^n$, which satisfies $\boldsymbol{A}\boldsymbol{x} = \boldsymbol{b}$ and $x_j > 0$ for all j. The dual problem is

$$\max_{\boldsymbol{y}\in Y_d} \boldsymbol{b}^T\boldsymbol{y}, \quad Y_d = \left\{\boldsymbol{y} \in \mathbb{R}^m \mid \boldsymbol{A}^T\boldsymbol{y} + \boldsymbol{s} = \boldsymbol{c}, \boldsymbol{s} \geq \boldsymbol{0}\right\} \tag{20}$$

where $\boldsymbol{s}$ is a vector of slack variables.

An interior point for (20) is a vector $\boldsymbol{y} \in \mathbb{R}^m$ satisfying $\boldsymbol{A}^T\boldsymbol{y} + \boldsymbol{s} = \boldsymbol{c}$ and $s_j > 0$ for all j. (20) is of the same form as (19), except that only the slack variables $\boldsymbol{s}$ are restricted to be positive. The components of $\boldsymbol{y}$ are free. Hence only the slack variables are subject to scaling in each step of the algorithm. An obvious advantage of (20) over (19) is that it suffices to compute a new $\boldsymbol{y}$ at each iteration, which satisfies $\boldsymbol{A}^T\boldsymbol{y} < \boldsymbol{c}$. Then we may put $\boldsymbol{s} = \boldsymbol{c} - \boldsymbol{A}^T\boldsymbol{y}$, and the linear constraints will be satisfied without accumulated loss of

accuracy.

The original problem (18) has many free variables which are duplicated in the standard form (19). The corresponding pairs of slack variables must equal zero, and thus, for this particular problem, there are no interior points for the dual form (20).

In analogy with the Simplex method the scaling methods begin by finding a feasible starting point, i.e. by searching for an interior point for the form (20). This is done by solving the associated problem

$$\max\left\{-y_{ar} \mid \boldsymbol{A}^T\boldsymbol{y} - \boldsymbol{e}\, y_{ar} + \boldsymbol{s} = \boldsymbol{c}, \boldsymbol{s} \geq \boldsymbol{0}\right\} \tag{21}$$

where $\boldsymbol{e} \in \mathbb{R}^n$ has all coordinates equal to 1. This is the so-called phase 1. For any $\boldsymbol{y}$ we get an interior starting point for (21) by choosing y_{ar} sufficiently large. If there are interior points for (20), phase 1 is stopped with $y_{ar} < 0$. However, if there are no interior points, phase 1 will converge towards a feasible, but not necessarily optimal point for (20), and phase 2 will never start. The trick is to modify phase 1 in order to obtain convergence towards a feasible and optimal point for (20). In [1] the objective function for the original problem is included with some weight in phase 1 in order to produce a *good* starting point such that fewer iterations are necessary in phase 2:

$$\max\left\{\boldsymbol{b}^T\boldsymbol{y} - M\, y_{ar} \mid \boldsymbol{A}^T\boldsymbol{y} - \boldsymbol{e}\, y_{ar} + \boldsymbol{s} = \boldsymbol{c}, \boldsymbol{s} \geq \boldsymbol{0}\right\}. \tag{22}$$

This is the so-called "big-M" method. In [3] the following modification is suggested:

$$\max\left\{\boldsymbol{b}^T\boldsymbol{y} - My_{ar} \mid \boldsymbol{A}^T\boldsymbol{y} - \boldsymbol{e}\, y_{ar} + \boldsymbol{s} = \boldsymbol{c}, \quad \boldsymbol{s} \geq \boldsymbol{0}, y_{ar} \geq 0\right\} \tag{23}$$

In (23) scaling is also applied to y_{ar} with the effect of adjusting the weight on the artificial variable y_{ar}. While the dual of (22) contains the constraint $\boldsymbol{e}^T\boldsymbol{x} = M$, which may be inconsistent, the dual of (23) only requires $\boldsymbol{e}^T\boldsymbol{x} \leq M$. It is shown in [3] that (23) is an improvement, both theoretically and computationally. It is proved that for a problem without interior points convergence is achieved in phase 1, i.e. by solving the associated problem (23). Phase 2 never starts.

4 Computational Results

The test problem is described in [9]. In the plane strain model a rectangular block of material is given infinitely thin symmetric external cuts of various depths. Figure 1 shows an orthogonal cross section of the rectangular block. The load distribution consists of a uniform tensile force applied at the end faces of the material. The Mises yield condition in plane strain is linearized using 16 linear inequality constraints at each node, introducing a linearization error of less than 2% on the collapse multiplier. The components of the stress tensor are discretized using piecewise constant functions, and the velocity components by piecewise bilinear functions, both over a uniform square grid. The problem size is reduced using the 2 symmetry axes.

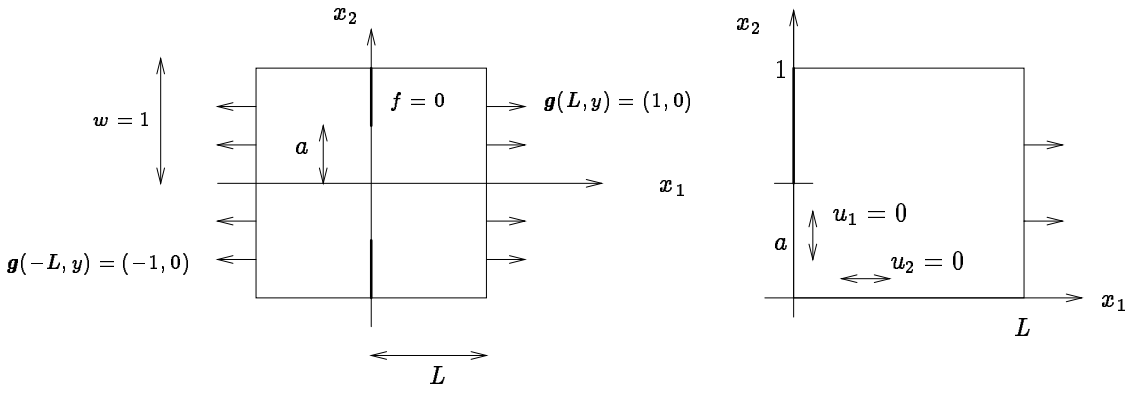

Figure 1: Geometry and symmetry reduction for the test problem in plane strain.

The largest case solved here corresponds to a 201×201 grid, compared to a 30×30 grid in [9]. Our solutions are more accurately determined in addition to being closer to the continuous solution due to the finer grid. They provide discrete collapse fields with more detail than seen before.

Table 1 lists some computed values for the collapse multiplier for three different depths of the cut, experimental convergence orders based on these values and the extrapolated values to order 1. (For precise definition and method see [10].) The results indicate that the error in the collapse multiplier satisfies

$$|\lambda_h^* - \lambda^*| \leq c\, h \tag{24}$$

	$a = 1/3$			$a = 1/2$			$a = 2/3$		
h^{-1}	λ_h^*	order	extr.	λ_h^*	order	extr.	λ_h^*	order	extr.
12	0.9826			1.2117			1.4826		
24	0.9584		0.9342	1.1776		1.1434	1.4400		1.3973
36	0.9493	0.79	0.9311	1.1656	0.90	1.1415	1.4250	0.90	1.3949
48	0.9448	1.01	0.9312	1.1596	1.03	1.1417	1.4177	1.11	1.3960
60	0.9421	0.97	0.9311	1.1561	1.07	1.1421	1.4134	1.03	1.3962
72	0.9403	1.19	0.9315	1.1537	0.82	1.1416	1.4104	0.73	1.3952
84	0.9391	1.08	0.9316	1.1519	0.97	1.1415	1.4082	1.08	1.3954
96	0.9381	1.08	0.9317	1.1506	0.96	1.1414	1.4066	1.00	1.3954
150	0.9359	1.10	0.9319	1.1473	1.02	1.1415	1.4025	0.90	1.3951
198	0.9349	1.06	0.9320						

Table 1: Results for $L = 1$, $a = \frac{1}{3}$, $a = \frac{1}{2}$ and $a = \frac{2}{3}$.

where h is the mesh size. However, it does not hold that

$$\lim_{h \to 0} \frac{\lambda_h^* - \lambda^*}{h} = c. \tag{25}$$

This is due to the fact that the solutions are non-smooth and is in agreement with [6]. Figure 2 shows the computed collapse multipliers for $L = 2$. (Triangles are used to indicate that the values based on the linearized yield condition constitute an upper bound relative to the exact convex Mises condition.)

The collapse fields for some representative solutions are shown in figures 3–5. In each figure part (a) visualizes the collapse deformation as follows: the collapse velocity at each node has been multiplied by a suitable time scale, and the resulting deformed grid is drawn. In part (b) of the figures a dot is used to indicate the elements in which the stress tensor (constant within each element) is at the yield surface, i.e. where the yield condition is active. This is the *plastified region*. In [9] a digit was used to indicate the direction of the stress tensor in the plastified region. Our grid is too fine for this, but the stresses are consistent with those of [9]. The main improvement in the solution fields is the higher

Figure 2: Computed values for the collapse multiplier for $L = 2$, $a = \frac{1}{3}$, $a = \frac{1}{2}$ and $a = \frac{2}{3}$.

resolution and detail. The deformation zone appears to be very thin, possibly infinitely thin, near the end of the cuts and then to spread somewhat, as it propagates into the material. In some cases non-plastified elements appear inside the plastified region. We believe this to be an artifact of the algorithm in combination with non-uniqueness and ill-conditioning.

There appears to be an oscillatory pattern of small deformations in the large non-plastified region which is known to be rigid by complementary slackness. This phenomenon was also seen in [6] and [9]. It is due to the non-uniqueness of solutions to the discrete problem. For the continuous problem it follows from (12) that $\boldsymbol{\varepsilon}(\boldsymbol{u}^*) = \mathbf{0}$, whenever $\boldsymbol{\sigma}^*$ is not at the yield surface. In the discrete analogue of (12) the maximum is taken only over those $\boldsymbol{\sigma}_h$ which are constant within each element, and hence the discrete version of the principle of complementary slackness only implies that $\boldsymbol{\varepsilon}(\boldsymbol{u}_h^*)$ vanishes in average over each element. The region is "discretely rigid".

It is apparent from these collapse fields that adaptive mesh generation must be used in practical applications. In limit analysis this is more tricky than in elasticity. In elasticity problems the deformation is uniquely determined and relatively smoothly distributed and

serves as an excellent indicator for mesh refinement. In the case of non-unique or poorly determined fields the mesh refinement algorithm can be expected to influence the final solution and thereby hide information. This point needs further investigation. In this paper our main objective has been to examine the power of the optimization algorithm.

In [3] the efficiency of our optimization algorithm is documented on the standard netlib set of test problems. For the problem in limit analysis presented here we can compare with the results in [9]. However, it must be emphasized that in [9] only little priority was given to efficiency; the qualitative properties of interior point methods, mainly the handling of ill-conditioning and the ability to determine the collapse fields, was given first priority. For all other algorithms, which we have tested on this problem, the factor limiting the grid size has been loss of accuracy due to ill conditioning, not cpu-time. The largest case solved in [9] was on a 30 by 30 grid, resulting in 9901 columns, 7280 rows and 52888 nonzeros. This took 18 iterations of the primal affine scaling method (using the conjugate gradient method in the projection step) and about 65 cpu-hours on a SUN-3/180 workstation with a Weitek 1164/1165 floating point accelerator board. Here we have solved the same problem on a 201 by 201 grid. After dualization this gave 687353 columns, 121204 rows, (81338 free variables in the primal problem), 2301985 nonzeros in initial matrix and about 10 times as many nonzeros in the Cholesky factor. The optimizer used 98 iterations and about 32 cpu-hours on a CONVEX C3240 (compiled with the full vectorization option). The accuracy, measured in feasibility and duality gap of the optimal solution, was of the order 10^{-7}.

5 Conclusion

The suggested solution algorithm, based on the Dual Affine Scaling Algorithm, allows computations in limit analysis with much finer grids than previously. This enables us to present solutions with a high degree of details, even with a uniform grid, and confirms the expected 1st order convergence of the collapse multiplier.

References

[1] I. Adler, N. Karmarkar, M.G.C. Resende and G. Veiga, An implementation of Karmarkar's algorithm for linear programming, *Mathematical Programming* **44** (1989), 297–335.

[2] E. Anderheggen and H. Knöpfel, Finite element limit analysis using linear programming, *Int. J. Solids Struct.* **8** (1972), 1413–1431.

[3] K.D. Andersen, An infeasible dual affine scaling method for linear programming, *Committee on Algorithms Bulletin* **22** (1993), 19–27.

[4] M. Capurso, Limit analysis of continuous media with piecewise linear yield condition, *Meccanica* **6** (1971), 53–58.

[5] R. Casciaro and A. DiCarlo, Mixed F.E. models in limit analysis, in: J.T. ODEN, ed., *Computational methods in nonlinear mechanics*, Austin, Texas (1974), 171–181.

[6] E. Christiansen, Computation of limit loads, *Int. J. Num. Meth. Engrg.* **17** (1981), 1547–1570.

[7] E. Christiansen, On the collapse solution in limit analysis, *Arch. Rational Mech. Anal.* **91** (1986), 119–135.

[8] E. Christiansen and K.O. Kortanek, Computing material collapse displacement fields on a CRAY X-MP/48 by the Primal Affine Scaling Algorithm, *Ann. Oper. Res.* **22** (1990), 355–376.

[9] E. Christiansen and K.O. Kortanek, Computation of the collapse state in limit analysis using the LP Primal Affine Scaling Algorithm, *J. Comp. Appl. Math.* **34** (1991), 47–63.

[10] E. Christiansen and H.G. Petersen, Estimation of convergence orders in repeated Richardson extrapolation, *BIT* **29** (1989), 48–59.

[11] N. Karmarkar, A new polynomial-time algorithm for linear programming, *Combinatorica* **4** (1984), 373–395.

Figure legends

Figure 1: Geometry and symmetry reduction for the test problem in plane strain.

Figure 2: Computed values for the collapse multiplier for $L = 2$, $a = \frac{1}{3}$, $a = \frac{1}{2}$ and $a = \frac{2}{3}$.

Figure 3a: Collapse deformation for $L = 1$, $a = \frac{1}{3}$ and $h = \frac{1}{198}$.

Figure 3b: Plastified region for $L = 1$, $a = \frac{1}{3}$ and $h = \frac{1}{198}$.

Figure 4a: Collapse deformation for $L = 1$, $a = \frac{2}{3}$ and $h = \frac{1}{150}$.

Figure 4b: Plastified region for $L = 1$, $a = \frac{2}{3}$ and $h = \frac{1}{150}$.

Figure 5a: Collapse deformation for $L = 2$, $a = \frac{1}{2}$ and $h = \frac{1}{100}$.

Figure 5b: Plastified region for $L = 2$, $a = \frac{1}{2}$ and $h = \frac{1}{100}$.